Editors' Suggestion

Efficient periodic density functional theory calculations of charged molecules and surfaces using Coulomb kernel truncation

Sudarshan Vijay,[1,*,†] Martin Schlipf,[1] Henrique Miranda,[1] Ferenc Karsai,[1] Merzuk Kaltak,[1] Martijn Marsman,[1] and Georg Kresse[1,2,‡]

[1]*VASP Software GmbH, Berggasse 21, 1090 Vienna, Austria*

[2]*Faculty of Physics and Center for Computational Materials Science, University of Vienna, Kolingasse 14-16, A-1090 Vienna, Austria*

(Received 6 January 2025; revised 29 April 2025; accepted 21 May 2025; published 10 July 2025)

Density functional theory (DFT) calculations of charged molecules and surfaces are critical to applications in electrocatalysis, energy materials, and related fields of materials science. DFT implementations such as the Vienna *ab initio* simulation package (VASP) compute the electrostatic potential under three-dimensional (3D) periodic boundary conditions, necessitating charge neutrality. In this work, we implement 0D and 2D periodic boundary conditions to facilitate DFT calculations of charged molecules and surfaces, respectively. We implement these boundary conditions using the Coulomb kernel truncation method. Our implementation computes the potential under 0D and 2D boundary conditions by selectively subtracting unwanted long-range interactions in the potential computed under 3D boundary conditions. By combining the Coulomb kernel truncation method with a computationally efficient padding approach, we remove nonphysical potentials from vacuum in 0D and 2D systems. To illustrate the computational efficiency of our method, we perform large supercell calculations of the formation energy of a charged chlorine defect on a sodium chloride (001) surface and perform long-timescale molecular dynamics simulations on a stepped gold (211)|water electrode-electrolyte interface.

DOI: 10.1103/cd6s-cdkf

I. INTRODUCTION

Efficient density functional theory calculations of charged molecules and surfaces are crucial to predict novel electrocatalysts [1,2], reliable battery materials [3,4], and stable defects at surfaces of semiconductors [5,6]. Commonly used DFT implementations such as the Vienna *ab initio* simulation package (VASP) [7] rely on periodic boundary conditions in all dimensions [three-dimensional (3D) boundary conditions]. While this assumption of periodicity allows for computationally efficient fast-Fourier transforms (FFT) to solve the Poisson equation (to compute the potential from a charge density), it imposes restrictions on the dimensionality of materials that can be computed without the influence of spurious electrostatic interactions from periodic replicas.

There are two constraints with using 3D boundary conditions to solve the Poisson equation. First, we implicitly assume that *both* the charge density and the resulting potential are periodic in all dimensions [8,9]. Bulk materials satisfy this criterion and are hence trivially treated by this method. Conversely, systems with lower dimensionality, such as 2D and quasi-2D systems (surfaces), 1D systems (nanowires), and 0D systems (molecules), are partially or fully nonperiodic and require large cells to remove spurious electrostatic interactions between unwanted periodic replicas [10–14]. Second, this reciprocal space method requires charge neutrality, i.e., the electronic and nuclear charges must sum to zero [8]. Total energies of systems that are not charge neutral are divergent and hence of limited use [9].

The first challenge of lower-dimensional periodicity has been approached by Coulomb kernel truncation techniques [12,14,15]. These methods adapt the Poisson equation to lower dimensionality. However, they require padded cells at least 27× larger than the conventional cells for 0D systems and 2× larger for 2D systems [14]. Padding makes this procedure computationally expensive, as FFTs scale with the supercell dimension N as $N \log N$. This expense precludes large supercell calculations and long-timescale *ab initio* molecular dynamics simulations. Recent implementations [12,15] circumvent the use of padding by requiring a large vacuum along the nonperiodic dimension. However, this choice leads to artifacts in the potential at the edges of the cell and requires convergence with respect to both vacuum dimension and choice of kernel truncation. Alternative approaches, such as modifying the basis functions to be nonperiodic in certain dimensions, prevent the need for padding, but require specialized treatments such as using

*Contact author: sudarshan.vijay@vasp.at; sudarshan.vijay@iitb.ac.in

†Present address: Department of Chemical Engineering, Indian Institute of Technology Bombay, Powai, Mumbai, Maharashtra 400076, India.

‡Contact author: georg.kresse@univie.ac.at

Published by the American Physical Society under the terms of the Creative Commons Attribution 4.0 International license. Further distribution of this work must maintain attribution to the author(s) and the published article's title, journal citation, and DOI.

the full-potential linearized augmented plane-wave (FLAPW) method [16].

The second challenge of charge neutrality has been addressed by applying a compensating homogeneous background charge over the entire cell followed by adding appropriate potential alignment terms [17]. Alternatively, a compensating charge is added to regions of the cell where there is a vanishing charge density, such as in the case of implicit solvent methods [2,18–20]. While this compensating charge may be physically motivated in certain applications, it often introduces additional artifacts into the computation of the total energy that must be treated *post facto* [21,22].

In this work, we solve both these challenges by implementing a method for applying established Coulomb kernel truncation methods for systems with 0D and 2D boundary conditions *without* the need for increased FFT grids. Our approach allows for computing large systems efficiently and is suitable for performing long-timescale molecular dynamics simulations. With this method, we treat charged 2D periodic surfaces, effectively removing the requirement of charge neutrality. Throughout this manuscript, we detail specifics of our method as implemented in VASP. In Sec. II, we review Coulomb kernel truncation methods to alter 3D boundary conditions to 0D and 2D boundary conditions. In Sec. III, we describe our approach of Coulomb truncation without padding to a large supercell. In Sec. IV, we compare the variation of the total energy between 3D, 2D, and 0D boundary conditions. In Sec. V, we illustrate the computational advantage of our approach by calculating the dependence of the formation energy on the concentration of charged vacancy defects of sodium chloride (NaCl). In addition, we perform charged *ab initio* molecular dynamics simulations of a stepped Au(211) | water interface over long timescales.

II. COULOMB KERNEL TRUNCATION AND CHARGED SYSTEMS

In this section, we compute the potential under 0D and 2D boundary conditions by truncating the Coulomb kernel [12,14,15]. We highlight modifications to the current 3D implementation of VASP and outline the procedure to compute the potential of charged surfaces and molecules without any *post hoc* corrections. As an illustration, we discuss differences in the computed potential through a representative example of charge-neutral and positively charged MoS_2 with and without applying the Coulomb kernel truncation method.

A. Coulomb kernels for 3D, 2D, and 0D boundary conditions

We determine the potential (V) from a given charge distribution (ρ) using the Poisson equation

$$V(\mathbf{r}) = \int \frac{\rho(\mathbf{r}')}{|\mathbf{r}-\mathbf{r}'|} d\mathbf{r}', \tag{1}$$

where $\mathbf{r}$ denotes a position in real space. In a fully periodic calculation, the integral in Eq. (1) is performed over all repeated cells and the periodic charge density $\varrho(\mathbf{r})$ as

$$V(\mathbf{r}) = \int \frac{\varrho(\mathbf{r}')}{|\mathbf{r}-\mathbf{r}'|} d\mathbf{r}'. \tag{2}$$

However, since the potential is also cell periodic, $\mathbf{r}$ can be restricted to the primitive cell. Fourier transforming Eq. (2) to reciprocal space, we get

$$V(\mathbf{g}) = \frac{4\pi}{\mathrm{g}^2} \varrho(\mathbf{g}), \tag{3}$$

where $\mathbf{g}$ is a reciprocal lattice vector. We use nonbold versions of the symbol (for example, g) to indicate the norm of the vector of the symbol (for example, $\mathbf{g}$). We introduce the Coulomb kernel v_{3D} as

$$v_{3D}(\mathbf{g}) = \begin{cases} 4\pi/\mathrm{g}^2, & \mathrm{g} \neq 0, \\ 0, & \mathrm{g} = 0, \end{cases} \tag{4}$$

to express Eq. (3) as

$$V(\mathbf{g}) = v_{3D}(\mathbf{g}) \varrho(\mathbf{g}). \tag{5}$$

Physically, applying this kernel to ϱ generates a potential where each point feels the entire $1/r$ Coulomb interaction from every other point in space.

We follow Ref. [15] and implement 0D and 2D periodic boundary conditions by restricting the Coulomb interaction to a certain region ($\mathcal{R}$)

$$v(\mathbf{r}) = \begin{cases} 1/r, & r \in \mathcal{R}, \\ 0, & r \notin \mathcal{R}. \end{cases} \tag{6}$$

For 0D boundary conditions, we truncate the kernel in real space to a sphere [14]

$$v(\mathbf{r}) = \frac{1}{r} \theta(R_\mathrm{c} - r), \tag{7}$$

where R_c is the radius of the sphere and θ is the Heaviside function. Similarly, $\mathcal{R}$ is a cuboid for 2D boundary conditions with the real-space kernel [12,15]

$$v(\mathbf{r}) = \frac{1}{r} \theta(R_\mathrm{c} - r_z). \tag{8}$$

Here, R_c is the dimension of the cuboid in the direction of the surface normal and r_z is the position along the surface normal. Solving the Poisson equation in reciprocal space, we require the Fourier-transformed kernels derived in Refs. [14,15] for 0D boundary conditions,

$$v_{0D}(\mathbf{g}) = \begin{cases} 4\pi/\mathrm{g}^2[1 - \cos(\mathrm{g}R_\mathrm{c})], & \mathrm{g} \neq 0, \\ 2\pi R_\mathrm{c}^2, & \mathrm{g} = 0, \end{cases} \tag{9}$$

and for 2D boundary conditions in Ref. [15],

$$v_{2D}(\mathbf{g}) = \begin{cases} 4\pi/\mathrm{g}^2[1 - e^{-\mathrm{g}_\parallel R_\mathrm{c}}(\cos(\mathrm{g}_\perp R_\mathrm{c}) - \mathrm{g}_\perp/\mathrm{g}_\parallel \sin(\mathrm{g}_\perp R_\mathrm{c}))], & \mathrm{g} \neq 0, \\ 4\pi/\mathrm{g}_\perp^2[1 - \cos(\mathrm{g}_\perp R_\mathrm{c}) - \mathrm{g}_\perp R_\mathrm{c} \sin(\mathrm{g}_\perp R_\mathrm{c})], & \mathrm{g}_\parallel = 0, \\ -2\pi R_\mathrm{c}^2, & \mathrm{g} = 0, \end{cases} \tag{10}$$

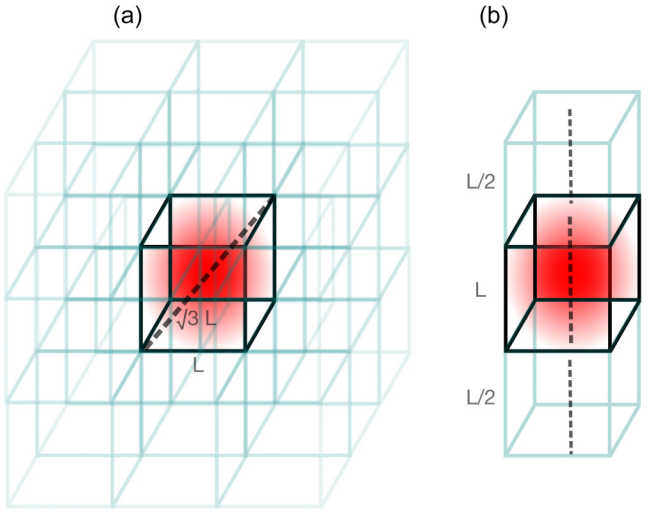


FIG. 1. Schematics showing the construction of padded supercells for (a) 0D boundary conditions and (b) 2D boundary conditions; the red sphere denotes the original charge density and the blue cells represent the padded cells.

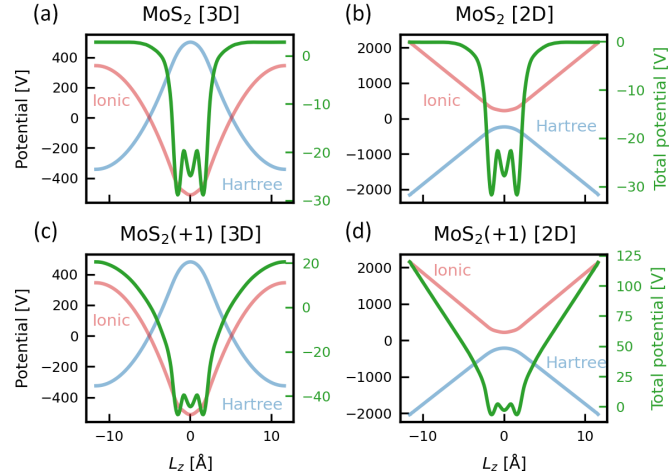


FIG. 2. Comparison of the Hartree, ionic, and total (sum of Hartree, ionic, and exchange-correlation) potential for (a) neutral MoS_2 with 3D boundary conditions, (b) neutral MoS_2 with 2D boundary conditions, (c) positively charged MoS_2 with 3D boundary conditions, and (d) positively charged MoS_2 under 2D boundary conditions. Tick labels for the total potential (green) are on the right.

where $g_\parallel$ is the norm of the $\mathbf{g}$ vector parallel to the surface and $g_\perp$ is the projection of the $\mathbf{g}$ vector on the surface normal. Note that, for the specific choice of $R_c = L_z/2$, the sin terms of Eq. (10) go to zero and there is no divergence at $g_\parallel \to 0$ (see the Appendix for further discussion) [23].

B. Constructing padded supercells

In the previous section, we presented Coulomb kernels for 0D and 2D dimensionalities which depend on a truncation parameter R_c. In this section, we discuss how R_c is chosen in practice for 0D and 2D dimensionalities. Note that the kernels can be applied to any of the supercells described in this section.

R_c must be sufficiently large such that the nonperiodic charge density, ρ, does not interact with its periodic counterpart across nonperiodic boundaries [12,15,24]. We prevent this spurious interaction by extending the region $\mathcal{R}$ in Eq. (6) to the edges of the cell and computing the Poisson equation in a padded supercell. By using a padded cell approach as opposed to simply applying v_{2D} and v_{0D}, we remove any contributions to the self-consistently determined local potential caused by spurious interactions with repeated images.

Figure 1 shows a schematic of the padded supercell used for 0D and 2D systems. For 0D boundary conditions, ρ [shown in red in Fig. 1(a)] must not interact with any of its periodic replicas. Padding the cell in every dimension [blue cells in Fig. 1(a)] fulfills this requirement but leads to a supercell that is $3^3 = 27$ times larger than the otherwise considered cell [15]. For 2D boundary conditions, ρ must not interact with its periodic replicas in the direction of the surface normal, requiring padding of $2\times$ the norm of the lattice vector along one dimension [blue cells in Fig. 1(b)] [12,15].

These padded cells lead to a potentially large computational cost associated with applying 0D and 2D boundary conditions in practice. We defer discussion of our method for applying 0D and 2D boundary conditions without the need for extended FFT grids to Sec. III.

C. Comparing 2D and 3D potential for charge neutral and charged systems

In this section, we compare the potential computed using 3D and 2D boundary conditions as discussed in Sec. II A. We illustrate the differences in 2D and 3D boundary conditions by computing the potential of a charge-neutral and positively charged single layer of MoS_2.

Figure 2 shows the electron-electron Hartree potential (in blue), ion-electron (in red), and the total potential, i.e., sum of Hartree, ionic, and exchange-correlation potentials (in green) for a single layer of charge-neutral and charged MoS_2 under 3D and 2D boundary conditions. The Hartree potential is obtained through Eq. (3) where ϱ is the valence charge density,

$$V_{\text{Hartree}}(\mathbf{g}) = v(\mathbf{g})\varrho(\mathbf{g}). \tag{11}$$

Note that $v(\mathbf{g})$ is replaced by $v_{2D}(\mathbf{g})$ or $v_{0D}(\mathbf{g})$ to compute the Hartree potential for 2D or 0D systems, respectively. As in the formulation of Ref. [25], the ionic potential is determined by setting ϱ to the ion charge as if they were point charges and adding the local contributions of the pseudopotential for each atom i, $U_{\text{ps,i}}$,

$$V_{\text{ionic}} = \sum_i \left(v(\mathbf{g})\frac{Z_i}{\Omega} + U_{\text{ps},i} \right), \tag{12}$$

where Z_i is the valence charge of each atom i and Ω is the volume. Note that we do not truncate the local pseudopotential as the corresponding charge density $(Z_i/\Omega + \varrho_{\text{ps},i})$ is short ranged and does not influence the potential beyond the atomic radius [12].

Under 3D boundary conditions, the Hartree and ionic potential [blue and red lines in Fig. 2(a), respectively] show

parabolic behavior in vacuum, i.e., they have L_z^2 dependence far away from the material. Conversely, the same system computed with 2D boundary conditions shows linear behavior in L_z [blue and red lines in Fig. 2(b)] of the potential in vacuum. When summed together for a neutral system [green lines in Figs. 2(a) and 2(b)], the parabolic and linear dependence on L_z is removed from 3D and 2D boundary conditions, respectively. The only difference in the two potentials is that the total potential decays to zero far away from the material under 2D boundary conditions, while it decays to an arbitrary value under 3D boundary conditions (value of the green lines at $L_z = \pm 10$).

This parabolic behavior of the Hartree and ionic potential under 3D boundary conditions stems from the convention of setting the $\mathrm{g} = 0$ term of the 3D Coulomb kernel to zero [17,25,26]. This choice implicitly represents solving the Poisson equation with the charge density set to the sum of ϱ and a compensating homogeneous background charge with magnitude equal to the negative of the total integral charge of ϱ. For charge-neutral systems, the homogeneous background charge contribution for the Hartree and ionic potentials cancel out (as they are of equal and opposite magnitudes) and the resulting total potential is free from parabolic behavior.

In contrast, the linear behavior of the Hartree and ionic potential under 2D boundary conditions is the appropriate behavior of a charged 2D sheet such as MoS_2. We expect a charged sheet of charge q and area A to have a potential of $2\pi z\, q/A$ where z is the distance along the surface normal [27]. This linear behavior is seen for both the Hartree and ionic potentials in Fig. 2(b) and no homogeneous background charge is applied in either case. For charge-neutral systems, this linear dependence is canceled out when the Hartree and ionic potentials are added together and, hence, the total potential decays to the reference value of zero in a vacuum.

Unlike charge-neutral systems, charged systems do not exhibit equivalent behavior of the total potential for 3D and 2D boundary conditions. In contrast to charge-neutral systems, the total potential under 3D boundary conditions [green line in Fig. 2(c)] exhibits parabolic dependence on L_z. This parabolic dependence is caused by the homogeneous background charge that is implicitly present when computing the total potential of a system that is not charge neutral. While the contributions to the total potential of the homogeneous background charge disappear for a charge-neutral system, it is present when summing the Hartree and ionic potential for a charged system under 3D boundary conditions [26]. There is no such parabolic dependence for the potential computed under 2D boundary conditions [green line in Fig. 2(d)]. Instead, a linear dependence of the potential commensurate with a charged 2D sheet is observed for the Hartree, ionic, and total potentials.

In summary, Fig. 2 shows that applying 2D boundary conditions for 2D materials allows us to compute the potential for charged systems. Applying 3D boundary conditions to charged 2D materials generates artifacts caused by the presence of a parabolic potential. We note that the homogeneous background charge is not actually enforced in 3D boundary condition calculations. Instead, the lack of inclusion of the $\mathrm{g} = 0$ terms of the potential [for example, in Eq. (4)] implicitly assumes that the total charge is zero, which in turn leads to a parabolic potential. If one were to Fourier transform (FT) the sum of the ionic and electronic charge from reciprocal space to real space and set the $\mathrm{g} = 0$ density term to zero before the FT, the homogeneous background charge would be clearly visible in the vacuum. And the solution of the Poisson equation ($\Delta V = 4\pi c$) is always a quadratic function in the region of constant charge c. In the case of 0D and 2D boundary conditions, the divergence of the 0D kernel (along all dimensions) and the 2D kernel (along the direction of the surface normal) as seen in Eqs. (9) and (10) is absent and there is no need to force the total density to be zero at $\mathrm{g} = 0$. Therefore, the "unphysical" parabolic behavior is also gone (see also the Appendix).

III. EFFICIENT PADDING FOR SURFACES AND MOLECULES

In Sec. II, we showed that applying the appropriate kernel and padding a cell with vacuum allows us to compute the potential for 0D and 2D boundary conditions. While these kernels can be applied to any cell, padded or unpadded, obtaining a potential without any spurious interactions is possible only through a padded supercell. A key challenge with applying this method is the need for computationally expensive padded cells. In this section, we discuss the computational bottlenecks with the currently used *padded supercell* method and present our *coarsen before padding* method, which performs kernel truncation without the need for enlarged FFT grids. We compare the two approaches against the *no-padding* method, which performs truncation without padding. We note that these padding and unpadding methods are applied for each self-consistent field cycle (SCF). This repeated use of either approach to generate the potential from the charge density implies that the overall cost of the calculation will benefit from a more computationally efficient method.

A. Padded supercell method

Algorithm 1 illustrates the padded supercell approach for determining the potential. First, the periodic charge density ϱ is padded to create a nonperiodic charge density ρ (Line 1, Algorithm 1). An FFT (denoted as $\mathcal{F}$) is performed on this padded cell to generate $\rho(\mathbf{g})$ (Line 2, Algorithm 1). As FFTs scale like $\mathcal{O}(N \log N)$, this FFT is the largest computational expense of this method [schematically shown in Fig. 3(a)]. For 0D systems, the padded cell is a grid of $3\mathrm{N} \times 3\mathrm{N} \times 3\mathrm{N}$ (in blue), where N is the number of points in the cell. This padded grid is 27 times larger than the original $\mathrm{N}\times\mathrm{N}\times\mathrm{N}$ grid (in green).

Following this expensive FFT, the padded potential $V_{\mathrm{pad}}(\mathbf{g})$ is computed using Eq. (5) with the appropriate kernel (Line 3, Algorithm 1). An inverse Fourier transform (denoted as $\mathcal{F}^{-1}$)

ALGORITHM 1. Padded supercell method.

1: $\rho(\mathbf{r}) = \mathrm{Pad}[\varrho(\mathbf{r})]$
2: $\rho(\mathbf{g}) = \mathcal{F}[\rho(\mathbf{r})]$
3: $V_{\mathrm{pad}}(\mathbf{g}) = v(\mathbf{g})\rho(\mathbf{g})$
4: $V_{\mathrm{pad}}(\mathbf{r}) = \mathcal{F}^{-1}V_{\mathrm{pad}}(\mathbf{g})$
5: $V(\mathbf{r}) = \mathrm{Unpad}[V_{\mathrm{pad}}(\mathbf{r})]$

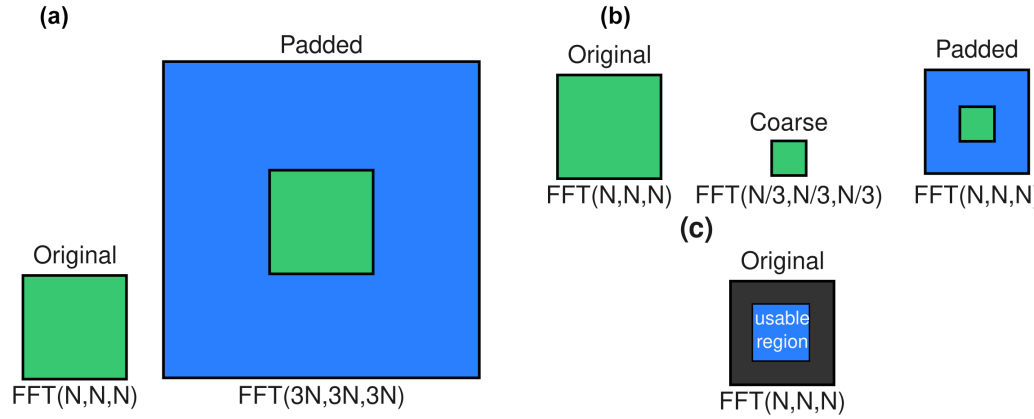


FIG. 3. Schematic of (a) padding supercell method using a larger grid, (b) coarsen before padding method that coarsens the original grid before padding, and (c) no-padding method which performs truncation without padding for a 0D system; the usable region shows where the potential obtained is the correct one.

converts it to real space, $V_{\text{pad}}(\mathbf{r})$ (Line 4, Algorithm 1). This inverse FFT is equally expensive as the FFT used to compute $\rho(\mathbf{g})$ (Line 2, Algorithm 1) and doubles the computational cost.

Finally, $V_{\text{pad}}(\mathbf{r})$ is condensed in real space to generate $V(\mathbf{r})$, i.e., grid points corresponding to the points in the original grid are retained while those corresponding to the padded grid are removed (Line 5, Algorithm 1).

B. Coarsen before padding method

Instead of computing the entire potential with 0D or 2D boundary conditions, our *coarsen before padding* method selectively subtracts away truncated components from a 3D periodic potential to achieve 0D or 2D boundary conditions. The sequence of steps to achieve this selective computation is as follows.

(1) Fourier transform the 3D periodic charge density and compute the periodic potential, V_{periodic} (Lines 1 and 2 of Algorithm 2). We will selectively subtract the truncated interactions from V_{periodic} at the end of the algorithm.

(2) Generate a coarse grid consisting of N/3×N/3×N/3 [see Fig. 3(b)] for 0D boundary conditions and N × N×N/2 for 2D boundary conditions, where N × N×N is the dimension of the original cell. Note that an unequal number of grid points is allowed by this method. Transfer elements of ϱ corresponding to this coarse grid to generate the coarse charge density, ρ_{coarse} (Lines 3–5 of Algorithm 2).

(3) Compute the 3D periodic potential of ρ_{coarse} to generate $V_{\text{periodic,coarse}}$ (Line 6 of Algorithm 2). This potential contains unwanted long-range periodic interactions included in V_{periodic} and will be subtracted from it.

(4) Perform the conventional padding procedure as seen in Algorithm 1 on ρ_{coarse} to generate V_{coarse} (Lines 8–9 of Algorithm 2). Note that, unlike Algorithm 1, there is no need to perform FFTs on an enlarged FFT grid as padding the coarsened cell returns the original FFT grid.

(5) Subtract from V_{periodic} the unwanted periodic interactions $V_{\text{periodic,coarse}}$ and add the correctly truncated interactions V_{coarse} to generate the potential under the required boundary conditions (Lines 10–11 of Algorithm 2).

The reasoning behind the present approach is loosely based on the Gaussian theorem, i.e., long-range electrostatics depend only on monopoles, dipoles, and higher-order poles. It is well understood that broadening the density, e.g., replacing a point charge with a Gaussian charge density, leaves the electrostatic potential unchanged beyond the radius where the Gaussian decays to zero [27]. Removing large $\mathbf{g}$ components from the density also preserves all electrostatic multipoles, thus completely preserving the long-range electrostatics. These reasons illustrate that the current approach is inherently free of any errors, which we will demonstrate below. In passing, we note that the FFT grids used to correct the errors in the long-range electrostatics could be further reduced, but, from an implementation point of view, the present strategy was easier to implement in VASP and a further reduction would only marginally increase the computational efficiency.

ALGORITHM 2. Coarsening before padding method.

1: $\varrho(\mathbf{g}) = \mathcal{F}[\varrho(\mathbf{r})]$
2: $V_{\text{periodic}}(\mathbf{g}) = 4\pi/\mathrm{g}^2\varrho(\mathbf{g})$
3: **if** $\mathbf{g} = \mathbf{g}_{\text{coarse}}$ **then**
4: $\quad\rho_{\text{coarse}}(\mathbf{g}_{\text{coarse}}) = \varrho(\mathbf{g}_{\text{coarse}})$
5: **end if**
6: $V_{\text{periodic,coarse}}(\mathbf{g}_{\text{coarse}}) = 4\pi/\mathrm{g}^2_{\text{coarse}}\rho_{\text{coarse}}(\mathbf{g}_{\text{coarse}})$
7: $\rho_{\text{coarse}}(\mathbf{r}_{\text{coarse}}) = \mathcal{F}^{-1}[\rho_{\text{coarse}}(\mathbf{g}_{\text{coarse}})]$
8: Apply Algorithm 1 to ρ_{coarse} to obtain $V_{\text{coarse}}(\mathbf{r}_{\text{coarse}})$
9: $V_{\text{coarse}}(\mathbf{g}_{\text{coarse}}) = \mathcal{F}[V_{\text{coarse}}(\mathbf{r}_{\text{coarse}})]$
10: $V(\mathbf{g}) = V_{\text{periodic}}(\mathbf{g}) - V_{\text{periodic,coarse}}(\mathbf{g}_{\text{coarse}}) + V_{\text{coarse}}(\mathbf{g}_{\text{coarse}})$
11: $V(\mathbf{r}) = \mathcal{F}^{-1}[V(\mathbf{g})]$

C. No-padding method

An alternative approach to truncating the Coulomb kernel is to avoid padding entirely [12,15]. This no-padding method implicitly assumes that the charge density decays to near zero at the boundary of the cell along the nonperiodic dimension. This assumption allows for truncation without padding with the explicit consideration that the potential generated at the

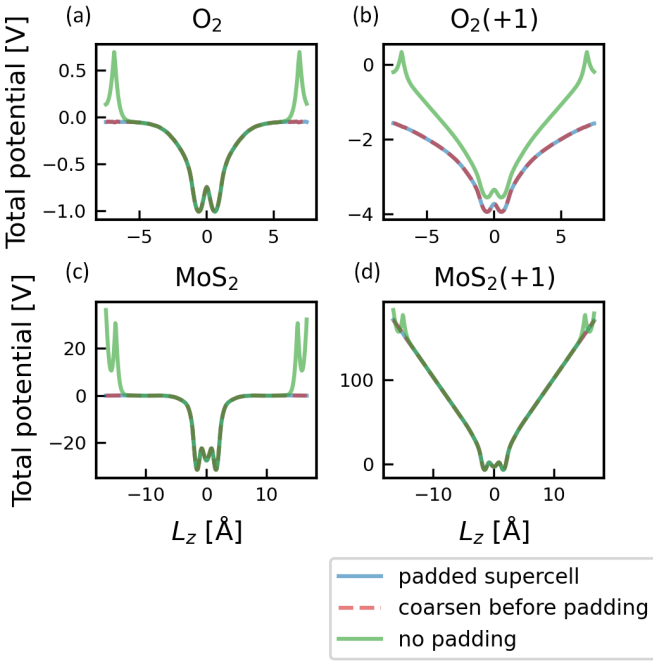


FIG. 4. Total potential generated by the padded supercell method (solid blue line), the coarsen before padding method (dashed red line), and the no-padding method (solid green line) (a) oxygen molecule, (b) positively charged oxygen molecule, (c) a single layer of MoS_2, and (d) a positively charged single layer of MoS_2.

edges of the cell are nonphysical and are to be ignored [dark regions of Fig. 3(c)]. This method is implemented by simply swapping out $v(\mathbf{g})$ for the appropriately truncated kernel.

D. Comparison of self-consistent potentials

Figure 4 shows that the total potential computed using the coarsen before padding method (dashed red lines) matches the total potential computed by the conventional padded supercell method (solid blue lines) for a charge-neutral and charged O_2 molecule and a single layer of MoS_2. This potential equivalence shows that we can achieve exactly the same accuracy for our DFT calculation without the need for expensive FFT operations on a larger FFT grid.

Both the coarsen before padding and the padded supercell method generate physical potentials throughout the cell. In contrast, the no-padding approach (green lines, Fig. 4) produces physical potentials when the charge density is nonzero (for example, at $L_z \approx 0$), but produces nonphysical potentials towards the cell boundaries ($L_z = \pm 6$ Å for O_2 and $L_z = \pm 12$ Å for MoS_2).

Note that the potentials of the no-padding approach are similar to the padded supercell and coarsen before padding potentials for the case of $MoS_2(+1)$, but appear slightly different for $O_2(+1)$. This deviation comes from the choice of R_c used for the no-padding approach. We set R_c to half the length of the largest norm of the lattice vectors (padded or otherwise) for MoS_2 and choose R_c as $\sqrt{3}$ times the cell for O_2 computed with the padded supercell method and coarsen before padding method. For O_2 computed with the no-padding approach, we set R_c as half the length of the largest norm of the lattice vectors. This choice is required for the no-padding approach as it does not pad the cell and hence R_c cannot be larger than 1.

Well-chosen R_c ensures that the nonphysical region is distinct from any charge density, preventing any unwanted interactions from taking place. However, this convergence with respect to R_c may not be possible, especially during molecular dynamics calculations involving "floppy" molecules which may move into regions of unphysical potential.

Given the excellent performance of our coarsen before padding method at a reduced computational cost as compared with the padded supercell method and the need for a physical potential throughout the cell, we set it as the default option for VASP calculations including Coulomb kernel truncation and use it for the rest of this manuscript.

IV. ENERGIES FOR 0D AND 2D BOUNDARY CONDITIONS

In Secs. II and III, we showed that using an appropriate Coulomb truncated kernel, we generate the Hartree, ionic, and total potentials for 0D and 2D boundary conditions. In this section, we briefly describe how these potentials are used to compute components of the total energy for charge-neutral and charged systems. We highlight modifications to VASP to facilitate total energy calculations with 0D and 2D boundary conditions.

For charged systems, 3D boundary conditions require potential alignment to generate meaningful energies [17]. This alignment is usually performed using either an explicit potential reference within the cell or through modifying the local-pseudopotential term to include interactions between a homogeneous background charge and the added (or subtracted) number of electrons [17,25]. As shown in the Appendix, 0D boundary conditions do not require potential alignment, but 2D boundary conditions do require alignment when taking energy differences between charged and uncharged systems.

A. Hartree energy

The electrostatic energy caused by electron-electron interactions (Hartree energy) is computed in reciprocal space as

$$E_{\text{Hartree}} = \frac{\Omega}{2} \sum_{\mathbf{g}} \rho(\mathbf{g}) V(\mathbf{g}), \tag{13}$$

where $V(\mathbf{g})$ is the potential under either 3D, 2D, or 0D boundary conditions as determined in Secs. II and III. The only change to the current VASP implementation is to supply $V(\mathbf{g})$ for the appropriate boundary condition to Eq. (13).

B. Sum of eigenvalues

The sum of the eigenvalues on a per-atom basis is

$$E_{\text{eigenvalues}} = \sum_{i} \epsilon_i, \tag{14}$$

where i is the running index over all computed eigenvalues with a nonzero occupancy. Equation (14) implicitly depends on the total potential as the numerical values of ϵ are determined by the potential in which they are computed.

For 3D boundary conditions, the value of the potential is arbitrary (as the g = 0 component of Hartree and ionic potentials are set to zero) and hence the values of ϵ are arbitrary as well. In contrast, for both 0D and 2D boundary conditions, we include the g = 0 component [as seen in Eqs. (9) and (10), respectively] explicitly. This implementation choice allows us to compute the absolute eigenvalues for charge-neutral molecules using the 0D boundary condition and surfaces using the 2D boundary condition. This output of the absolute eigenvalues implies that properties such as the work function of 2D surfaces are immediately available and do not require a potential reference within the cell.

C. Ion-ion interaction energy

As done for the 3D boundary condition implementation in VASP, we compute the ion-ion interaction energies using the Ewald summation technique. The total summation of ion point charges on a lattice is split into a real space (short-range) component and a reciprocal space (long-range) component with some additional analytical terms

$$E_{\text{ion-ion}} = E_{\text{long-range}} + E_{\text{short-range}} + E_{\text{self}} + E_{\text{homogeneous}}, \quad (15)$$

where $E_{\text{long-range}}$ is the long-range energy, $E_{\text{short-range}}$ is the short-range energy, E_{self} is the energy of self-interaction between the smeared charge and the point charge of the Ewald sum, and $E_{\text{homogeneous}}$ is the energy of interaction between the point charge and a homogeneous background charge.

For 0D boundary conditions, we set $E_{\text{short-range}}$, E_{self}, and $E_{\text{homogeneous}}$ to zero and compute the entire ion-ion interaction energy in real space. We choose this direct computational strategy as there is no periodicity and hence no need for long-range interaction terms, self-correction, and homogeneous background charge terms

$$E_{\text{ion-ion}} = \frac{1}{2}\sum_{i\neq j}\frac{Z_i Z_j}{r_{ij}}, \quad (16)$$

where r_{ij} is the distance between any two atomic charges with index i and j and Z_i and Z_j are the corresponding atomic charges.

For 2D boundary conditions, we implement the 2D Ewald summation to compute the terms in Eq. (15) as per the formulation of Ref. [28], which includes terms for $E_{\text{long-range}}$, $E_{\text{short-range}}$, and E_{self}, while setting $E_{\text{homogeneous}}$ to zero. The long-range part is

$$E_{\text{long-range}} = \frac{\pi}{2A}\sum_{i,j} Z_i Z_j \sum_{\text{g}\neq 0}\cos(\mathbf{g}\cdot\mathbf{r}_{ij})\left[\frac{\exp(\text{g}z)\text{erfc}[\alpha z + \text{g}/(2\alpha)] + \exp(-\text{g}z)\text{erfc}[-\alpha z + \text{g}/(2\alpha)]}{\text{g}}\right], \quad (17)$$

where A is the surface area, z is the distance between i and j in the direction of the surface normal, and α is the splitting parameter between long- and short-range summations. We do not change the default value of α used by VASP, which is inversely proportional to the cube root of the volume of the cell. The short-range energy is computed similarly to 3D boundary conditions,

$$E_{\text{short-range}} = \frac{1}{2}\sum_{i,j}{}' Z_i Z_j \sum_{\mathbf{n}}\frac{\text{erfc}\left(\alpha|\mathbf{r}_{ij}+\mathbf{n}|\right)}{|\mathbf{r}_{ij}+\mathbf{n}|}, \quad (18)$$

where $\mathbf{n}$ is the index of the real space cell and the prime over the first summation indicates that the sum does not include terms where $i = j$ and $\mathbf{n} = 0$. The self-correction term is

$$E_{\text{self}} = -\frac{\alpha}{\sqrt{\pi}}\sum_{i=1}^{N} Z_i^2 - \frac{2\pi}{A}\sum_{i,j} Z_i Z_j\left[z\,\text{erf}(\alpha z) + \frac{\exp[-(z\alpha)^2]}{\alpha\sqrt{\pi}}\right], \quad (19)$$

where N is the number of atoms. The term in square brackets is an additional self-correction term for systems with a nonzero height parallel to the surface normal or systems that are not charge neutral.

D. Validation

We test our implementation by computing the self-consistent Hartree energy, eigenvalues, ion-ion energies, and total energies for a charge-neutral and positively charged pyridene molecule under 0D boundary conditions and charged single-layer MoS_2 sheet under 2D boundary conditions. We describe the behavior of these energies with a change in lattice vectors along all directions for pyridene and along the surface normal (i.e., amount of vacuum) for MoS_2.

1. Charge-neutral pyridine molecule

Figure 5 shows the (negative of) the Hartree energy, sum of the eigenvalues, ion-ion and total energies for pyridine under 3D boundary conditions (in orange), 2D boundary conditions (in blue), and 2D boundary conditions with no padding (in green) with change in the vacuum in the cell (x axis is the inverse of the vacuum lattice dimension, z). Applying 0D boundary conditions leads to energies that are invariant to the amount of vacuum in the cell, i.e., all blue points are equivalent. In contrast, Hartree energies, eigenvalues, and the ion-ion energies computed by the 3D boundary conditions are dependent on the choice of vacuum. This dependence on the vacuum size exactly cancels for total energies of charge-neutral materials [Fig. 5(d)]. This match of the total energy between the 0D and 3D boundary conditions [blue and orange points overlap in Fig. 5(d)] shows that our implementation yields identical results to the 3D implementation when sufficient vacuum is used for charge-neutral species.

Finally, we compare the total energies of the coarsen before padding and the no-padding method. We find that the coarsen before pad method converges with less vacuum in the cell than the no-padding method [total energies at $1/L_z = 0.1$ Å^{-1} in Fig. 5(d)]. This faster convergence with vacuum dimension

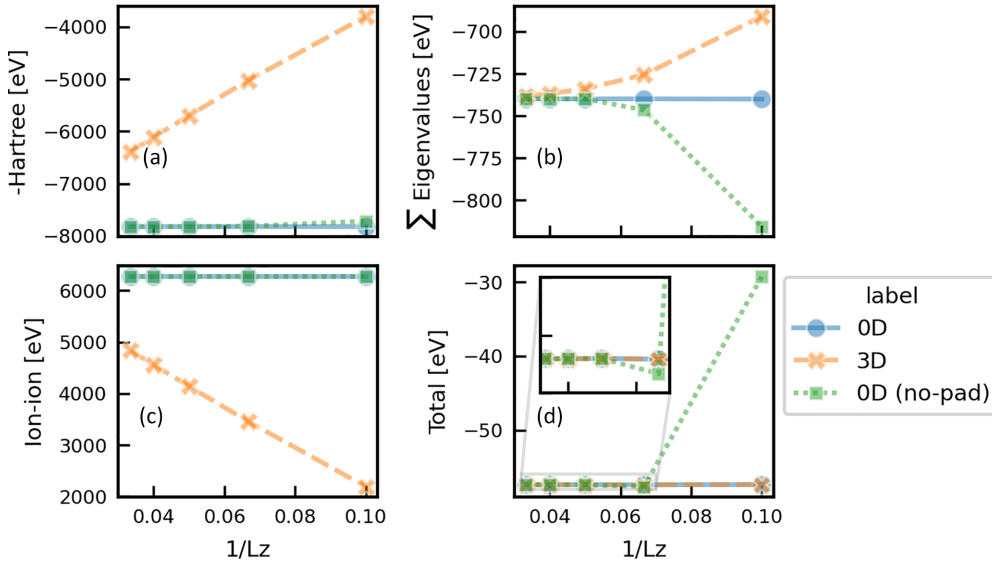


FIG. 5. Variation of energy contributions for a charge-neutral pyridine molecule: (a) negative of the Hartree energy, (b) sum of the eigenvalues, (c) ion-ion energy, and (d) total energy; orange points and lines indicate that 3D boundary conditions were used, blue points and lines indicate 0D boundary conditions were used, and green points and lines indicate that 0D boundary conditions using the no-padding method were used. The inset shows a zoom-in of the total energies.

implies that the coarsen before padding method can be used with less vacuum in the cell for 0D systems. Besides the reduced computational cost due to a smaller vacuum dimension (fewer g vectors along the aperiodic dimension), the self-consistent electrostatic potential with the 0D and 2D boundary conditions contains no artifacts due to the dipole-dipole interactions across the nonperiodic dimension. This artifact-free potential allows us to compute the work function without the need for a dipole correction [10].

2. Positively charged pyridene molecule

Analogous to Fig. 5, Fig. 6 shows the variation of the Hartree, eigenvalue, ion-ion, and total energies of a charged pyridene molecule. In contrast to a charge-neutral pyridene molecule, Fig. 6(d) shows that the total energies are not equivalent for 0D (blue), 0D without padding (green), and 3D (orange). Under 3D boundary conditions, all individual energy contributions [Figs. 6(a), 6(b), and 6(c)] as well as the total energy [Fig. 6(d)] do not converge with increasing

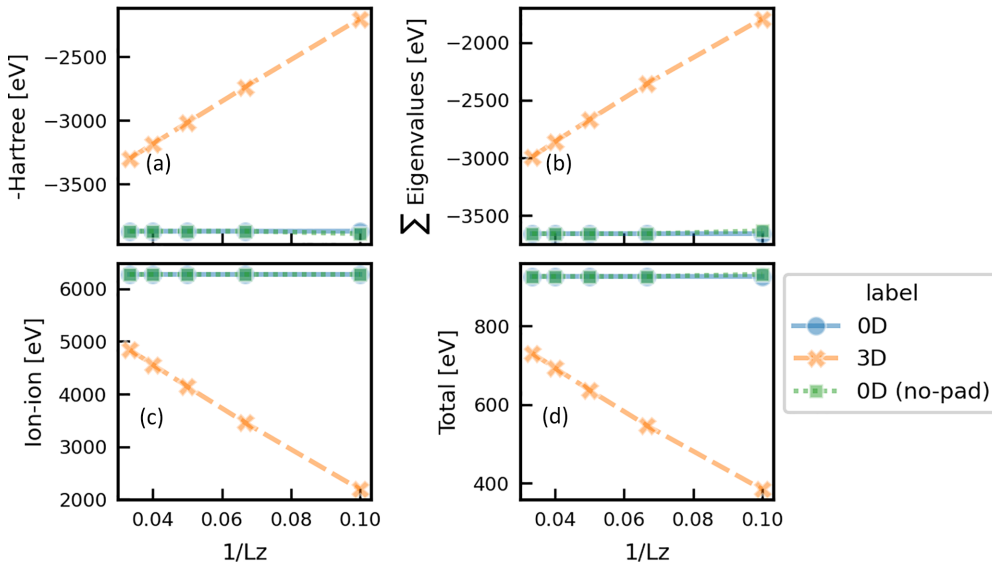


FIG. 6. Variation of energy contributions for a positively charged pyridine molecule: (a) negative of the Hartree energy, (b) sum of the eigenvalues, (c) ion-ion energy, and (d) total energy; orange points and lines indicate that 3D boundary conditions were used, blue points and lines indicate 0D boundary conditions were used, and green points and lines indicate that 0D boundary conditions using the no-padding method were used.

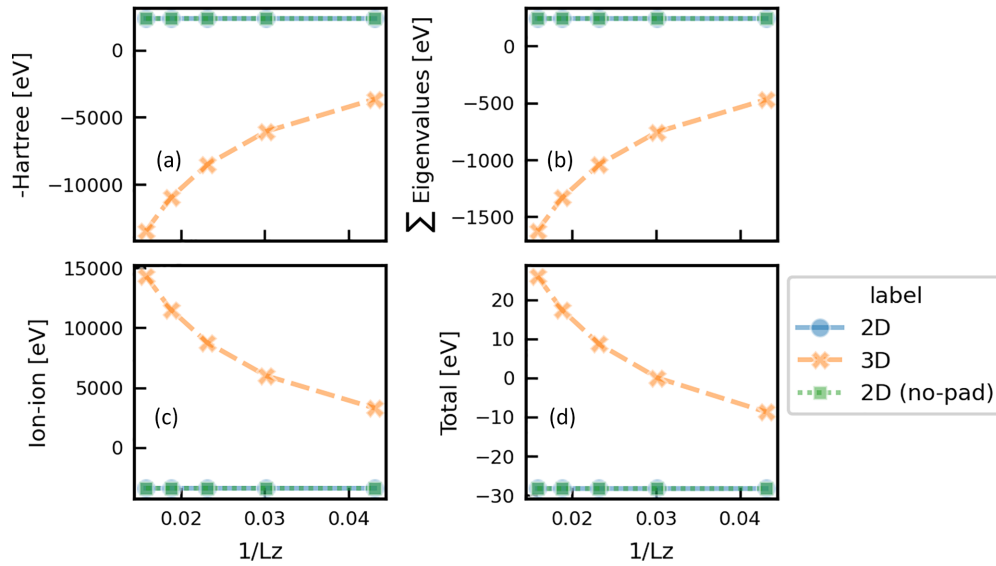


FIG. 7. Variation of energy contributions for a charged MoS_2 sheet: (a) negative of the Hartree energy, (b) sum of the eigenvalues, (c) ion-ion energy, and (d) total energy; orange points and lines indicate 3D boundary conditions were used, blue points and lines indicate 2D boundary conditions were used, and green points and lines indicate that 2D boundary conditions using the no-padding method were used.

cell dimension. Applying 0D boundary conditions, either with or without padding, leads to converged energies at all cell dimensions (x axis).

3. *Positively charged* MoS_2 *sheet*

A key difference between the energies computed with 3D and 2D boundary conditions is the convergence behavior of the total energies for positively charged MoS_2 (Fig. 7). The total energy [Fig. 7(d)] is identical for all vacuum sizes when computed using 2D boundary conditions (blue and green points). In contrast, the total energies diverge when computed with 3D boundary conditions [orange points in Fig. 7(d)], i.e., they increase with increasing vacuum size and never converge to a single value. This divergence of the total energy stems from the inability of 3D boundary conditions to balance the individual divergences of the Hartree energy [orange points, Fig. 7(a)], eigenvalues [orange points, Fig. 7(b)], and ion-ion energy [orange points, Fig. 7(c)]. In comparison, the Hartree energies, sum of eigenvalues, and ion-ion and total energies computed with 2D boundary conditions show no divergence [blue and green points in Figs. 7(a), 7(b), and 7(c)].

We note that the success of the 2D method to provide consistent energies is in part related to the choice that the potentials at the center of the slabs converge to one value independent of the vacuum width, whereas the potential at large distances diverges (as L_z). This behavior of the potential means that the work for adding or removing a charge quanta from a slab is always infinite, consistent with simple electrostatic arguments [27], and the divergence of the energies for the 3D case. The cost to generate a 2D charged slab is always infinite, but it is still possible to compare the stability of different charged 2D structures. This comparison is simplified using our implementation of 2D boundary conditions.

In summary, we find that self-consistent calculations with 0D and 2D boundary conditions for charge-neutral and charged surfaces provide consistent energies. This behavior is in contrast to performing calculations with 3D boundary conditions, which lead to convergent energies for charge-neutral surfaces but divergent energies for charged molecules and surfaces.

V. APPLICATIONS

In this section, we apply our implementation of the Coulomb kernel truncation method to two prototype cases of charged DFT calculations. Specifically, we compute the concentration dependent formation energy of a chlorine defect on NaCl(001) and the total energies and potential profile from a long-timescale machine-learning assisted Au(211) | water interface. Both illustrations would be particularly expensive with the padded supercell method due to either a requirement for large cells or long-timescale simulations.

A. Formation energy of a charged defect on a surface

To illustrate the difference between 3D and 2D boundary conditions, we compute the concentration-dependent formation energy of a prototypical charged defect, a chlorine vacancy defect on a surface of NaCl(001).

Formation energies of charged defects on surfaces show strong dependence on the concentration of the defects and vacuum when computed with 3D boundary conditions [5,6,29,30]. Several methods have been proposed to remove this dependence on the concentration and vacuum [29,30]. In general, these methods generate a surrogate model (typically a Gaussian charge density around the defect) in successively larger cells and extrapolate the energy to the limit of infinitely large vacuum and infinitely small defect concentration [29].

In this section, we show that the concentration and vacuum-dependent formation energy for charged defects computed under 2D boundary conditions show comparatively simple behavior, leading to a simpler extrapolation scheme using a quadratic least squares fit.

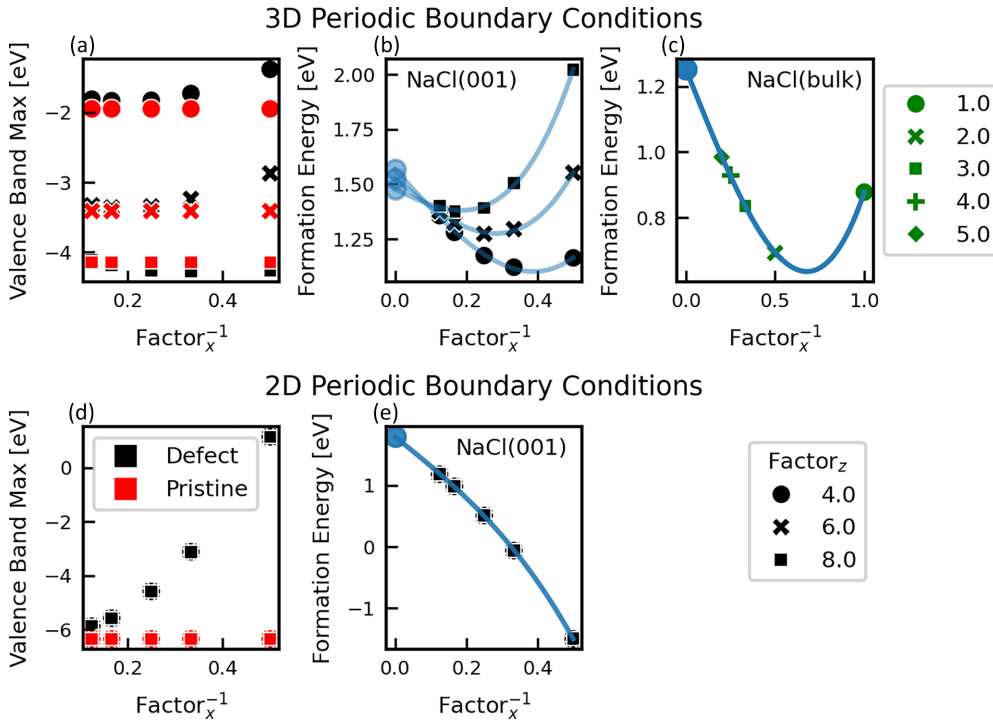


FIG. 8. Valence band maximum (VBM) computed under (a) 3D and (d) 2D boundary conditions. Black markers denote the VBM of the NaCl Cl-vacancy charged defect and red points correspond to the VBM of the uncharged pristine surface. Formation energies of the charged defect calculated under (b) 3D and (e) 2D boundary conditions. There is no dependence on the vacuum dimension with 2D boundary conditions (overlapping markers). Blue solid lines show the least squares fit for a cubic function. (c) Formation energy of a charged Cl-vacancy defect in bulk NaCl; blue solid line shows the least squares fit for a function of $1/L + 1/L^3$. Root mean square errors for the least square fits are 0.004 eV for surface defects [blue line in (d)] and 0.0001 eV for bulk defects [blue line in (e)]. The extrapolated value is shown as a blue dot in (b), (c), and (e). Markers indicate changing vacuum size through a multiplicative factor of the norm of the lattice vector along the z-direction Factor$_z$ (see main text for details).

The formation energy of a charged defect of Cl in NaCl(001) is

$$E_f[\mathrm{Na}_n\mathrm{Cl}_{n-1}(+1)] = E[\mathrm{Na}_n\mathrm{Cl}_{n-1}(+1)] - E[\mathrm{Na}_n\mathrm{Cl}_n] + \tfrac{1}{2}E[\mathrm{Cl}_2(\mathrm{g})] + q(\epsilon_v + \epsilon_F), \quad (20)$$

where E_f is the formation energy, $E[\mathrm{Na}_n\mathrm{Cl}_{n-1}(+1)]$ is the total energy of the charged defect with n Na species and $n-1$ Cl species, $E[\mathrm{Na}_n\mathrm{Cl}_n]$ is the total energy of the pristine host (without the defect) for n Na and Cl species, $E[\mathrm{Cl}_2(\mathrm{g})]$ is the chemical potential for the missing chlorine species between the host and the defect, and ϵ_F is the Fermi energy which is referenced to the valence band maximum (VBM) ϵ_v of the pristine surface (i.e., without a defect). We perform potential alignment (similar to that performed with 3D boundary conditions) of the formation energies by referencing them to ϵ_v. As we are interested in the general behavior of the formation energy with concentration and vacuum, we set $\epsilon_F = 0$. Any other value of ϵ_F would be a constant offset of the energies reported in this section.

Figure 8 illustrates differences in the behavior of the valence band maximum (VBM) and formation energies of the charged defect (denoted as $X^{q=1}$) as a function of the defect concentration and vacuum size (markers) computed under 3D and 2D boundary conditions. The defect concentration is modified by introducing a single chlorine defect within increasingly larger simulation cells (the x axis in Fig. 8 represents the lateral repetition factor Factor$_x$ of the primitive unit surface cell in the x and y directions). Furthermore, the vacuum size is altered by changing the cell dimension along the surface normal (markers in Fig. 8; Factor$_z$ is the total length of the lattice vector along the vacuum dimension in multiples of the lattice constant).

Figure 8(a) shows the VBM of a surface charged defect (black points) and of the pristine surface (red points) as a function of decreasing surface concentration of the defect computed with 3D boundary conditions. Consistent with the arbitrary offset of the potential with 3D boundary conditions, we find that the VBM is different for different surface concentrations (x axis) and different vacuum sizes (markers). There is no clearly extrapolatable trend as a function of different cell dimensions. Figure 8(d) shows the VBM computed with 2D boundary conditions. In contrast to Fig. 8(a), we find that the VBM has no dependence on vacuum size (overlapping black points) and decays to the VBM of the uncharged surface (red points). This behavior of the VBM is consistent with the reduced concentration of the charge as Factor$_x^{-1}$ goes to zero. In this case, using 2D boundary conditions leads to extrapolatable and intuitive behavior of the VBM of charged defects.

Formation energies do not converge with cell size [Fig. 8(b)] when computed under 3D boundary conditions. As a result, there is no clear trend between the formation energy and the defect concentration. *Post facto* methods that treat

the interaction of the charged defect with different concentrations with the homogeneous background charge [5,29,30] are needed to determine the formation energy.

In contrast, formation energies computed with 2D boundary conditions converge with decreasing surface concentration [Fig. 8(e)]. Furthermore, there is no dependence of the formation energies on the vacuum [markers in Fig. 8(e)]. This comparatively straightforward behavior suggests that extrapolation techniques can be used to determine the formation energy of the charged defect under infinitely dilute concentration.

To validate our approach of computing formation energies using 2D boundary conditions, we extrapolate the energies to $\text{Factor}_x^{-1} \to 0$ and compare our results against previously published work [30]. We fit the formation energies shown in Fig. 8(e) (black points) by least squares fitting a third-order polynomial (without the quadratic term) and extrapolate it to $\text{Factor}_x^{-1} \to 0$ [blue curve in Fig. 8(e)]. Our rationale for choosing linear and cubic terms is to effectively account for monopole-monopole, dipole-dipole interactions and any potential alignment terms, which are likely to be the leading terms in the dependence of the energy on the change in the defect concentration. The cubic terms are influenced by the potential alignment terms, which are proportional to the inverse volume, analogous to charged defects computed under 3D boundary conditions [17]. We find the formation energy at infinitely dilute concentrations to be 1.78 eV, which is very similar to the value of 1.89 eV computed by extrapolating formation energies using 3D boundary conditions and a model charge distribution [30]. The root mean square error (RMSE) of the fit is 0.004 eV, suggesting that our effective model of monopole-monopole, dipole-dipole interactions and potential alignments terms are sufficient to describe the interactions between charged defects on a surface.

We performed the same cubic fit for the vacuum dependent formation energies determined by 3D boundary conditions in Fig. 8(b) (blue lines). Similar to previously reported results for bulk charged defects, the formation energies do follow a $1/L + 1/L^3$ trend [17]. However, the extrapolated formation energies are also dependent on the vacuum dimension. They vary from 1.568 eV for $\text{Factor}_z = 4$, to 1.525 eV for $\text{Factor}_z = 6$, and 1.478 eV for $\text{Factor}_z = 8$.This vacuum-dependent behavior is in contrast to the vacuum-independent behavior of the extrapolated formation energies using 2D boundary conditions in Fig. 8(e).

Figure 8(c) shows a fit including linear and cubic terms, i.e., $1/L + 1/L^3$ (blue line) for a charged Cl-vacancy defect in bulk NaCl. We compute its formation energy under 3D boundary conditions. Similar to the surface defect in Fig. 8(e), we expect the leading concentration-dependent terms to be monopole-monopole, dipole-dipole, and potential alignment terms; the monopole-dipole terms are zero for NaCl as it is an isotropic system. We find that the least squares error for this fit is 0.0001 eV, suggesting a good fit between this simple model and the computed formation energies. Extrapolating this fit to $1/L \to 0$ leads to a formation energy at infinitely dilute concentrations of 1.25 eV, which is similar to the value of 1.50 eV obtained using a model charge distribution [30].

In summary, the formation energy of a surface-charged defect of chlorine on an NaCl(001) surface displays very different behavior with decreasing defect concentration and vacuum size for 3D and 2D boundary conditions. For 3D boundary conditions, both the VBM and the formation energies do not converge and require special methods to compute both of these quantities in the infinitely dilute concentration limit. In contrast, both the VBM and the formation energies display convergent behavior for calculations performed with 2D boundary conditions. This convergent behavior simplifies extrapolating formation energies to the infinite dilute concentration limit.

B. Electrode electrolyte interface

A key advantage of the coarsen before padding method is that the computational cost is roughly the same as for the equivalent 3D boundary condition calculation. This advantage allows us to perform *ab initio* molecular dynamics calculations for charged systems using 2D boundary conditions. To illustrate this advantage, we train a machine-learned force field (see Sec. VI) using more than 2400 DFT calculations with 2D boundary conditions for a system of 15 water molecules interacting with an Au(211) surface. We train two distinct force fields—one that is charge neutral and one with an added excess charge of $0.25e$.

Figure 9(a) shows the cumulative average energies (solid lines) and instantaneous energies (translucent lines) of a 1 nanosecond (ns) NVT molecular dynamics calculation for uncharged (blue) and charged (green) water Au(211) interface. The energies of both trajectories are stable for both charge-neutral and charged systems, i.e., the cumulative energies do not fluctuate. The charge-neutral system has a lower total energy due to the presence of more electrons and differences in the computed potential.

Figure 9(b) shows the z-averaged electrostatic potential for 100 evenly spaced structures from the 1 ns molecular dynamics trajectory. The charge-neutral potential (blue) decays to zero in the vacuum region ($z \approx 20$ Å). This flattening of the electrostatic potential to zero suggests that the averaged orientation of the water molecules is mostly random, i.e., the dipoles of water do not specifically orient along a certain axis. In cases where water had a specific mean orientation, we would expect the averaged electrostatic potential to decay to a nonzero value, with the potential at both ends ($z = \pm 10$ Å) settling at different values.

The z-averaged electrostatic potential increases linearly for a charged simulation cell [green lines in Fig. 9(b)]. This behavior of the potential for the charged system is similar to that of the charged plate potential of Fig. 2 and is a consistent feature of applying 2D boundary conditions to charged systems, irrespective of the thickness of the material [27].

Comparison of the electrostatic potentials of the charged and uncharged slab in Fig. 9(b) shows that the addition of a small amount of charge creates a field that is completely shielded by the aqueous electrolyte layer: the electrostatic potentials with and without charge almost perfectly align in the region of the aqueous electrolyte (0–10 Å), suggesting that the linear potential slope (visible between 10 and 20 Å) is entirely screened. In other words, the mesoscopic E field $E = D - 4\pi P$ is practically zero in the water layer. This screening is in line with the large dielectric constant of

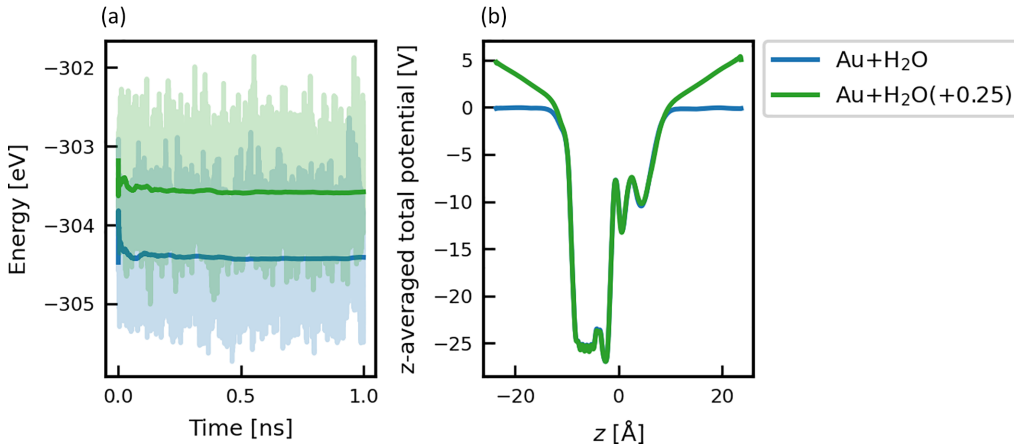


FIG. 9. (a) Total energy for each time step (transparent lines) and cumulative average (solid lines) for a (blue) charge neutral and (green) positively charged Au(211)|water interface (b) *xy*-averaged total potential for 100 evenly spaced snapshots from a 1 ns trajectory. The potential for the charged surface (green lines) has been moved to overlap with that of the uncharged (blue) electrostatic potential.

bulk water of 78.4 and implies that, in the water layer, the polarization almost exactly observes $P = D/4\pi$. This result also means that the water molecules reorient compared to the uncharged field-free case. A more detailed analysis is beyond the scope of the present work, albeit there is clearly interesting physics to unravel with the present approach.

In summary, we applied the Coulomb kernel truncation method to study the formation energy of charged defects and performed long-timescale molecular dynamics simulations of water over a charge-neutral and charged Au(211) surface. We find that our implementation provides a natural basis in which to compute properties of charged surfaces.

Given the convergent behavior for charged systems and the comparatively low computational cost of our implementation, we envision this Coulomb kernel truncation implementation to provide a starting point for further method development for computing properties of charged molecules and surfaces.

VI. METHODS

All density functional theory calculations were performed with the Vienna *ab initio* simulation package (VASP) [7]. The Coulomb kernel truncation method is implemented in VASP and is available as of version 6.5.0.

Charged defect calculations were performed on a single chlorine defect of NaCl(001). The structure, cell, and volume of bulk NaCl were relaxed using the `ISIF=3` option implemented in VASP using the PBE functional with a *k*-point sampling of $12\times12\times12$, yielding a lattice constant of $a = 3.93$ Å and $c = 5.56$ Å. The `Na_pv` and `Cl` PAW potential were used for Na and Cl atoms, respectively. A plane-wave cutoff of 262 eV was used for all charged defect calculations. The *k*-point density was kept constant for different defect concentrations on NaCl(001) by dividing the number of repetitions of the cell by 12, i.e., a 6×6 *xy* repetition of the cell was computed with a $2\times2\times1$ *k*-point sampling. Gaussian smearing was used with a broadening on 0.1 eV for all calculations. Similar to Ref. [30], no surface relaxation was performed for the defect, as we are interested in visualizing qualitative differences between 3D and 2D boundary conditions.

Molecular dynamics simulations of a 3×3 Au(211) surface with 4 Au layers in contact with an interface of water (3 layers with a total of 15 water molecules) were performed with an *NVT* ensemble. The lattice constant of Au ($a = 4.17$ Å) was determined based on the same computational setup as used for the molecular dynamics simulations. The `Au`, `O`, and `H` PAW potentials were used for Au, O, and H species, respectively. The bottom two layers were fixed in position throughout the simulation to mimic bulk Au. The temperature was controlled using the Nose-Hoover [31] thermostat. The mass of hydrogen in all simulations was set to 8 a.u.

We train a machine-learned force field (kernel-based method implemented in VASP) [32] to generate long-timescale simulation trajectories. Training structures to the force field were generated on the fly using the RPBE [33] functional with D3 [34] dispersion correction and zero damping. The temperature for both training runs was set to 300 K for the first 1800 training structures and then set to 350 K for the remaining structures. The training error for charge-neutral Au(211)|water is 1.15 meV/atom for the total energies and 77.9 meV/Å for the forces with 2445 DFT computations. The training error for positively charged (with a charge of 0.25 electrons removed) Au(211)|water interface is 1.27 meV/atom for the total energies and 76.0 meV/Å with 2822 DFT computations.

Postprocessing of all potential profiles used in this manuscript was performed with `py4vasp` and visualization was performed with `matplotlib`.

VII. CONCLUSIONS

In this work we describe our implementation of the Coulomb kernel truncation in the VASP package. Our implementation allows one to perform DFT calculations under 0D and 2D boundary conditions for neutral and charged systems. Instead of solving the Poisson equation to determine the potential on a computationally expensive vacuum-padded supercell, our approach subtracts only the relevant long-range contributions from the potential obtained in 3D boundary conditions. By using this method of determining the potential, our approach is only marginally more computationally expensive

than calculations using 3D boundary conditions. The present approach could easily be adopted for calculations of the exact exchange potential in Hartree-Fock or hybrid functional calculations, where we expect it to have an even greater impact than in the present case. We note that we have been rather modest with the grid coarsening in the present work, as for density functional theory the calculation of the potential is usually not a dramatic bottleneck. However, the coarsening can be increased significantly without loss of accuracy, since only electrostatic multipoles need to be described on the coarse grid.

We have applied our method to calculate the formation energy of a charged chlorine defect on a NaCl(001) surface. We find that the VBM and formation energy diverge when computed with 3D boundary conditions, but converge when computed with 2D boundary conditions. This allows reliable Cl vacancy formation energies to be extrapolated from the slab calculations. The extrapolated formation energy shows very good agreement with previous calculations. Furthermore, we demonstrate the computational efficiency of our implementation by performing nanosecond timescale molecular dynamics simulations of the Au(211) | water interface, with an excess charge located on the Au slab. This approach allows us to generate the long-range electrostatic field required to mimic an electrode. We believe that the present approach is well suited to determine structural changes induced by the finite field at an electrode. In fact, we observe that the water molecules rearrange in order to fully screen the displacement field induced by the Au electrode.

ACKNOWLEDGMENTS

S.V., M.S., M.M., and G.K. acknowledge support from EuroHPC Joint Undertaking for awarding us access to Leonardo at CINECA, Italy. This research was funded in part by the Austrian Science Fund (FWF) (Grant DOI: 10.55776/COE5).

The authors contributed as follows. S.V.: conceptualization, data curation, formal analysis, investigation, software, methodology, validation, visualization, writing—original draft, and writing—review and editing. M.S.: software, visualization, and writing—review and editing. H.M.: formal analysis and writing—review and editing. F.K.: formal analysis and writing—review and editing. M.K.: formal analysis, software, and writing—review and editing. M.M.: formal analysis, software, and writing—review and editing. G.K.: conceptualization, funding acquisition, investigation, methodology, software, resources, and writing—review and editing.

All authors of this manuscript are fully or partially employed by the VASP Software GmbH and are developers of the Vienna *ab initio* software package. G.K. is the main shareholder of the VASP Software GmbH.

DATA AVAILABILITY

The data that support the findings of this article are openly available [35].

APPENDIX: REFERENCING POTENTIALS

This manuscript discusses the variation of the energies of a 0D or 2D material with a change in cell dimension. We are often interested in energy differences, for example, computing the formation energies of charged defects in Sec. V. When taking these energy differences, we need to reference the potentials of these individual calculations to ensure compatibility between the separate DFT calculations. This potential referencing scheme (so-called potential alignment) has been discussed elsewhere for applications in charged defects [17,29] and electrochemistry [36]. In this section, we discuss the divergences in the kernels which necessitate potential alignment in our implementation.

There is no potential alignment required for calculations performed for 0D boundary conditions. The kernel [Eq. (9)] has no divergences for $g \to 0$ and the limit exists, i.e., it provides the same limit when approached from all directions.

Potential alignment is required for the case of 2D boundary conditions. The limit of the kernel [Eq. (10)] for $g_\parallel \to 0$ and $g_\perp \neq 0$ is

$$\lim_{g_\parallel \to 0, g_\perp \neq 0} v_{2D}(\mathbf{g}) = \lim_{g_\parallel \to 0, g_\perp \neq 0} \frac{4\pi}{g_\perp^2}[1 - \cos(g_\perp R_c) - g_\perp R_c \sin(g_\perp R_c)] + \frac{4\pi}{g_\perp^2}\left[\frac{g_\perp}{g_\parallel}\sin(g_\perp R_c)\right], \tag{A1}$$

where the last term in square brackets diverges. This divergence is countered by setting $R_c = L_z/2$, where L_z is the norm of the lattice vector along the aperiodic dimension. This choice of R_c causes the divergent term to go to zero [as $\sin(\pi) = 0$] [23] and is required for charged systems. For other choices of R_c, the $g \to 0$ limit does not exist for 2D boundary conditions because the value of the limit is $-2\pi R_c^2$ when approached from $g_\parallel \to 0$ and then $g_\perp \to 0$ and is infinite when we take the $g_\parallel \to 0$ limit in Eq. (A1). Analogous to the 3D boundary conditions, this divergent term is set to zero in our implementation and cancels out for charge-neutral systems when summing the Hartree and ionic potentials. For charge neutral systems, R_c can take any value as the divergent term cancels when summing the ionic and Hartree potentials (which are used to compute the individual energy contributions).

For charged systems, this divergence implies that the average electrostatic potential (equal to the $g = 0$ component) is undefined. This undefined nature of the average potential is in line with the increasing xy-averaged potential seen with charged 2D boundary conditions [for example, Fig. 2(d)]. It is this behavior of the average potential generated from the 2D kernel that requires potential alignment. Our choice of $g = 0$ in this manuscript is in keeping with previous work [15], which sets the potentials at the boundary of the cell along the aperiodic dimension to zero (for nondipolar systems). This choice is simply a convention and alternative choices [12] would produce the same results.

[1] S.-J. Shin, D. H. Kim, G. Bae, S. Ringe, H. Choi, H.-K. Lim, C. H. Choi, and H. Kim, On the importance of the electric double layer structure in aqueous electrocatalysis, Nat. Commun. **13**, 174 (2022).

[2] P. Lindgren, G. Kastlunger, and A. A. Peterson, Electrochemistry from the atomic scale, in the electronically grand-canonical ensemble, J. Chem. Phys. **157**, 180902 (2022).

[3] E. W. C. Spotte-Smith, R. L. Kam, D. Barter, X. Xie, T. Hou, S. Dwaraknath, S. M. Blau, and K. A. Persson, Toward a mechanistic model of solid-electrolyte interphase formation and evolution in lithium-ion batteries, ACS Energy Lett. **7**, 1446 (2022).

[4] N. Kumar, K. Leung, and D. J. Siegel, Crystal surface and state of charge dependencies of electrolyte decomposition on $LiMn_2O_4$ cathode, J. Electrochem. Soc. **161**, E3059 (2014).

[5] H. P. Komsa, N. Berseneva, A. V. Krasheninnikov, and R. M. Nieminen, Charged point defects in the flatland: Accurate formation energy calculations in two-dimensional materials, Phys. Rev. X **4**, 031044 (2014).

[6] C. Freysoldt, B. Grabowski, T. Hickel, J. Neugebauer, G. Kresse, A. Janotti, and C. G. Van de Walle, First-principles calculations for point defects in solids, Rev. Mod. Phys. **86**, 253 (2014).

[7] G. Kresse and J. Furthmüller, Efficient iterative schemes for *ab initio* total-energy calculations using a plane-wave basis set, Phys. Rev. B **54**, 11169 (1996).

[8] P. P. Ewald, Die Berechnung optischer und elektrostatischer Gitterpotentiale, Ann. Phys. (Leipzig) **369**, 253 (1921).

[9] S. W. de Leeuw, J. W. Perram, and E. R. Smith, Simulation of electrostatic systems in periodic boundary conditions. I. Lattice sums and dielectric constants, Proc. R. Soc. Lond. A **373**, 27 (1980).

[10] L. Bengtsson, Dipole correction for surface supercell calculations, Phys. Rev. B **59**, 12301 (1999).

[11] J. Neugebauer and M. Scheffler, Adsorbate-substrate and adsorbate-adsorbate interactions of Na and K adlayers on Al(111), Phys. Rev. B **46**, 16067 (1992).

[12] T. Sohier, M. Calandra, and F. Mauri, Density functional perturbation theory for gated two-dimensional heterostructures: Theoretical developments and application to flexural phonons in graphene, Phys. Rev. B **96**, 075448 (2017).

[13] G. Makov and M. C. Payne, Periodic boundary conditions in *ab initio* calculations, Phys. Rev. B **51**, 4014 (1995).

[14] M. R. Jarvis, I. D. White, R. W. Godby, and M. C. Payne, Supercell technique for total-energy calculations of finite charged and polar systems, Phys. Rev. B **56**, 14972 (1997).

[15] C. A. Rozzi, D. Varsano, A. Marini, E. K. Gross, and A. Rubio, Exact Coulomb cutoff technique for supercell calculations, Phys. Rev. B **73**, 205119 (2006).

[16] Y. Mokrousov, G. Bihlmayer, and S. Blügel, Full-potential linearized augmented plane-wave method for one-dimensional systems: Gold nanowire and iron monowires in a gold tube, Phys. Rev. B **72**, 045402 (2005).

[17] S. Lany and A. Zunger, Assessment of correction methods for the band-gap problem and for finite-size effects in supercell defect calculations: Case studies for ZnO and GaAS, Phys. Rev. B **78**, 235104 (2008).

[18] O. Andreussi and N. Marzari, Electrostatics of solvated systems in periodic boundary conditions, Phys. Rev. B **90**, 245101 (2014).

[19] K. Mathew, R. Sundararaman, K. Letchworth-Weaver, T. A. Arias, and R. G. Hennig, Implicit solvation model for density-functional study of nanocrystal surfaces and reaction pathways, J. Chem. Phys. **140**, 084106 (2014).

[20] R. Sundararaman, W. A. Goddard, and T. A. Arias, Grand canonical electronic density-functional theory: Algorithms and applications to electrochemistry, J. Chem. Phys. **146**, 114104 (2017).

[21] J. S. Hub, B. L. De Groot, H. Grubmüller, and G. Groenhof, Quantifying artifacts in Ewald simulations of inhomogeneous systems with a net charge, J. Chem. Theory Comput. **10**, 381 (2014).

[22] J. A. Gauthier, C. F. Dickens, H. H. Heenen, S. Vijay, S. Ringe, and K. Chan, Unified approach to implicit and explicit solvent simulations of electrochemical reaction energetics, J. Chem. Theory Comput. **15**, 6895 (2019).

[23] S. Ismail-Beigi, Truncation of periodic image interactions for confined systems, Phys. Rev. B **73**, 233103 (2006).

[24] N. D. M. Hine, J. Dziedzic, P. D. Haynes, and C.-K. Skylaris, Electrostatic interactions in finite systems treated with periodic boundary conditions: Application to linear-scaling density functional theory, J. Chem. Phys. **135**, 204103 (2011).

[25] J. Ihm, A. Zunger, and M. L. Cohen, Momentum-space formalism for the total energy of solids, J. Phys. C **12**, 4409 (1979).

[26] I. Dabo, B. Kozinsky, N. E. Singh-Miller, and N. Marzari, Electrostatics in periodic boundary conditions and real-space corrections, Phys. Rev. B **77**, 115139 (2008).

[27] J. D. Jackson, *Classical Electrodynamics*, 3rd ed. (Wiley, New York, 1999).

[28] D. M. Heyes, M. Barber, and J. H. R. Clarke, Molecular dynamics computer simulation of surface properties of crystalline potassium chloride, J. Chem. Soc. Faraday Trans. 2 **73**, 1485 (1977).

[29] C. Freysoldt, J. Neugebauer, and C. G. Van De Walle, Fully *Ab initio* finite-size corrections for charged-defect supercell calculations, Phys. Rev. Lett. **102**, 016402 (2009).

[30] H. P. Komsa and A. Pasquarello, Finite-size supercell correction for charged defects at surfaces and interfaces, Phys. Rev. Lett. **110**, 095505 (2013).

[31] S. Nosé, A unified formulation of the constant temperature molecular dynamics methods, J. Chem. Phys. **81**, 511 (1984).

[32] R. Jinnouchi, J. Lahnsteiner, F. Karsai, G. Kresse, and M. Bokdam, Phase transitions of hybrid perovskites simulated by machine-learning force fields trained on-the-fly with Bayesian inference, Phys. Rev. Lett. **122**, 225701 (2019).

[33] B. Hammer, L. B. Hansen, and J. K. Nørskov, Improved adsorption energetics within density-functional theory using revised Perdew-Burke-Ernzerhof functionals, Phys. Rev. B **59**, 7413 (1999).

[34] S. Grimme, Semiempirical GGA-type density functional constructed with a long-range dispersion correction, J. Comput. Chem. **27**, 1787 (2006).

[35] S. Vijay, Efficient periodic density functional theory calculations of charged molecules and surfaces using Coulomb kernel truncation [Data set], Zenodo (2025), https://doi.org/10.5281/zenodo.15494936.

[36] R. Jinnouchi, F. Karsai, and G. Kresse, Absolute standard hydrogen electrode potential and redox potentials of atoms and molecules: machine learning aided first principles calculations, Chem. Sci. **16**, 2335 (2025).